DRAFT
CMS Physics Analysis Summary

The content of this note is intended for CMS internal use and distribution only

Search for long-lived neutral particles decaying to photons with missing energy in proton-proton collisions at $\sqrt{s} = 8$ TeV

The CMS Collaboration

Abstract

A search for long-lived neutral particles decaying into a photon and an un-detectable particle such as gravitino, is performed using 19.1 fb^{-1} of proton-proton collision data at $\sqrt{s} = 8$ TeV. We present a method which exploits its long-lived feature by using the time measurement from the CMS Electromagnetic calorimeter. The method is sensitive to a range of lifetimes (τ) from 1.6 ns to 34 ns and is nearly free standard model background. Taking the Gauge Mediated Supersymmetry Breaking model as a benchmark and applying our method to the data, no significant excess is observed above background expectation. An exclusion region of neutralino mass and lifetime at 95% C.L. is set.

1 Introduction

The observation of the 125 GeV neutral boson at the LHC provides strong evidence for the Higgs mechanism of the standard model (SM). Despite the many successes of the standard model, the theory suffers from fine-tuning problems stemming from the Higgs sector [1] and has no explicit prediction for the unification of the gauge couplings and the role of gravity. With solutions for these questions, supersymmetry (SUSY) is one of the most compelling theories beyond the standard model. In addition, the Lightest Supersymmetric Particle (LSP) can be a stable particle making it a good candidate for dark matter. This scenario further motivates searches for the evidence of SUSY.

In the model of Gauge Mediated Suppersymmetry Breaking (GMSB) [2], the gravitino ($\tilde{G}$) is the LSP. Under the assumption of R-parity conservation [3], the gravitino is stable and couple weakly to the other SUSY particles. Strongly interacting supersymmetric particles with higher masses, such as the squarks and gluinos produced in proton-proton collisions at the LHC, provide large cross sections for SUSY production while at the same time through their prompt decays allow for lighter SUSY particles to be produced. The Next-to-Lightest Supersymmetric Particle (NLSP) is considered, in this analysis, to be the lightest of the promptly produced SUSY particles initiated by squark or gluino decays.

The NLSP for a range of GMSB model parameters will decay in a non-prompt manner, into the gravitino and SM particle(s). Depending on the choice of mass parameters, the NLSP can be a neutralino ($\tilde{\chi}_0$), stau or sneutrino. The mass, decay modes and lifetime of the NLSP depends on the SUSY breaking scale (Λ). If the NLSP is the neutralino, it has three different two-body decay channels with the gravitino produced with a photon, Z boson or a Higgs boson. The branching ratio (BR) for each channel depends on the choice of SUSY parameters. In this study, we choose the 'Snowmass Points and Slopes 8' (SPS8) [4] scenario as our benchmark model. In this scheme, the neutralino decay to a photon and a gravitino has the largest branching ratio [5](Table 1). Its lifetime is proportional to

$$\tau \propto \frac{M_P^2 m_{\tilde{G}}^2}{m_{\tilde{\chi}_0}^5} \tag{1}$$

Λ (TeV)	BR
100	0.9444
120	0.9042
140	0.8711
160	0.8464
180	0.8282
220	0.8043

Table 1: The branching ratio of $\tilde{\chi}^0 \to \gamma + \tilde{G}$

where M_P is the Plank mass. The neutralino mass ($m_{\tilde{\chi}^0}$) and the gravitino mass ($m_{\tilde{G}}$) are related to the SUSY breaking scale Λ. For example, the gravitino mass is given by

$$m_{\tilde{G}} = \frac{c_{grav}\Lambda M}{\sqrt{3}M_p} \tag{2}$$

where M is the mass of the messenger particle responsible for mediating SUSY breaking from the so-called *hidden sector* to a much lower energy scale where SUSY breaking is felt and c_{grav} is

a free parameter which influences the gravitino mass thus adjusting the lifetime of neutralino for a given energy scale. In this search, we focus on non-prompt decay of the neutralino. When the decay lifetime of the neutralino is sufficiently long, the arrival time of the resulting photon can be measurably later than normal prompt photons from proton interactions and this can be used to search for neutralino decays. We explore the parameter space covering possible neutralino lifetimes from 1 ns to 30 ns at different SUSY breaking scale.

The neutralinos are produced mainly when squarks or gluinos are pair produced. The cascade decay chain of a squark or gluino will lead to a neutralino as the NLSP and other quarks in the final state. Many of these events should have at least one late arriving photon, a few jets as well as missing energy from un-detectable gravitino. This is because many of the neutralinos are slow moving and when their flight lengths are long enough, the arrival time of the photons arising from the neutralino decays are measurably later than normal photons.

CMS electromagnetic calorimeter (ECAL) consists of 75848 $PbWO_4$ scintillation crystals, and with its fine granularity and excellent timing as well as energy resolution, it is a powerful tool to search for delayed photon signal. In addition, the absence of any known SM physics process at the TeV energy scale proton-proton collisions which would produce delayed photon, makes it possible to use ECAL timing measurements to perform a search with nearly zero background. Previous searches [6–9] has set the neutralino mass lower limits as high as 250 GeV/c^2 for different lifetime ranges between 0.25 ns to 50 ns.

2   Data and Monte Carlo samples

The data used in the analysis were collected during the 2012 runs with an integrated luminosity of 19.1 fb^{-1}. They are selected by an off-line trigger processor (HLT) which requires at least one isolated ECAL cluster (a collection of crystals with associated energy deposit) with E_T greater than 65 GeV and E_T^{miss} greater than 25 GeV.

The signal Monte Carlo (MC) samples are generated by PYTHIA 6 [10] with an external SLHA (Supersymmetry Les Houches Accord) file which describes SUSY parameters and mass spectrum. Those parameters are calculated by ISAJET [11]. The generation for signal samples adopts SUSY GMSB scheme where Λ, and c_{grav} are varied to cover a range (1.67 ns to 34 ns) of neutralino lifetime. The SUSY breaking scale, Λ, ranges from 100 TeV to 220 TeV where this analysis is most sensitive to according to the predicted cross-sections from GMSB.

The $\gamma+$ jets samples simulate photon radiated from a quark in the QCD process. The events are generated in different transverse momentum ranges with respect to the quark (denoted as $\hat{p}_T$). These samples are just used to study timing calibration and resolution in MC and data. Background arises from mis-measured collision events so-called spike hits (section 6.3), and beam-halo and cosmic ray-induced processes. Since their contributions must be estimated using data sample, we do not use any Monte Carlo sample for this purpose.

3   Event and Object Selection

As described briefly in section 1, neutralinos are pair produced from the cascade decays of two sparticles. As a result, our signal events are expected to have at least one photon and at least two jets. Another common feature in various models is the missing energy. Since gravitino is undetectable, significant amount of missing energy is expected. A cut on Missing Transverse Energy (E_T^{miss}) is useful to lower the rate from the standard model backgrounds like $\gamma+$ jets process and QCD events.

Photons are reconstructed using clustering algorithm to build a cluster of clusters (supercluster) [12], which extends cluster size in ϕ in order to recover energy spread due to strong magnetic field for photons which convert in positron-electron pairs. We use only photons from ECAL barrel in this analysis. We require that the transverse momentum (p_T) of the leading photon of the event must be greater than 80 GeV and other photon candidates must have p_T greater 45 GeV. Because particle-flow (PF) algorithm [13] considers off-timing photon as part of isolation energy deposit, the out-of-time photon will not be particle-flow isolated. As a result, we do not implement PF isolation critera for photon objects but require no tracks around the selected photon within $\Delta R = 0.6$ range and corresponding HCAL energy deposit less than 5 percent of ECAL energy deposit.

For jets and E_T^{miss} reconstruction, PF algorithm is used because it takes all sub-detectors information into account to reconstruct each particle before jet clustering. The PF jets are found to have highest purity and lowest fake rate to pass the jet quality cretira [14]. In this analysis, we select PF jets pass p_T threshold of 35 GeV and $|\eta| < 2.4$. A $\Delta R = \sqrt{\Delta\phi^2 + \Delta\eta^2}$ separation between a jet and a photon should be at least 0.3 to avoid counting the same object as a photon and jet.

PF ignores out-of-time energy deposits from ECAL crystal from E_T^{miss} calculation and includes it as anti-isolation energy deposits if it is part of photon cluster. In this analysis, since they are legitimate part of events, the photon E_T needs to be included in the E_T^{miss} calculations. Therefore, we correct the E_T^{miss} for events with out-of-time photons by subtracting the photon E_T vector from the E_T^{miss} vector. On the other hand, out-of-time photons from background sources do not belong to the event. If taking them into account for E_T^{miss} calculation of otherwise small E_T^{miss} collision event, the E_T^{miss} will be back to back with photon p_T and be the same in magnitude. Therefore, we define a variable called $E_{T\,no\gamma}^{miss}$ which is the vector sum of E_T^{miss} and photon E_T. For signal events, $E_{T\,no\gamma}^{miss}$ is also large unless the p_T sum of two gravitinos is back-to-back with photon E_T. Table 2 shows how events arising from various sources behave in terms of these two variables effectively. A threshold of 60 GeV for the E_T^{miss} and $E_{T\,no\gamma}^{miss}$ is found to suppress QCD and non-collision backgrounds.

Event Type	E_T^{miss}	$E_{T\,no\gamma}^{miss}$
Signal	Large	Large
W or Top events	Large	Large
QCD events	Small	Large
Non-collision backgrounds	Large	Small
Low p_T non-collision backgrounds	Small	Small

Table 2: E_T^{miss} and $E_{T\,no\gamma}^{miss}$ signature of different types of events.

In summary, our signal events should have at least one photon and at least two jets. The two ways to estimate the missing transverse energy, E_T^{miss} and $E_{T\,no\gamma}^{miss}$, are required to be greater than 60 GeV. Zero and one jet events are dominated by background and are particularly useful to study various sources of them.

4   ECAL Timing and Delayed Photon

The photon arrival time in ECAL is the main observable we use to distinguish signal from background in this study. The arrival time is estimated from 10 pulse-height measurements recorded every 25 ns over a 250 ns period from before and until after normal photons hit ECAL. The rising part of the shaped pulse depends on the relaxation time of the $PbWO_4$ crystal scintil-

lation process, while the falling part of the pulse is determined by the front-end electronics time constants. The pulse timing relative to the clock pulse uniquely determines the ratio of pulse heights from two consecutive measurements, we invert this relationship and use pulse height ratio to estimate the pulse timing relative to the LHC beam clock which is delivered to each crystal. Typically, samples 1 through 3 are pedestals, so the useful ratios are sample 4/sample 5, through sample 7/sample 8. The remaining ratios arising from the tail part of the pulse are not very sensitive to the pulse timing. We calculate weighted average of typically 3 measurements of pulse timing obtained this way as the pulse timing for each crystal. Even though the uncertainty in the ratio measurements is anti-correlated, its effect on the crystal timing estimate turns out to be less than 10% of the uncertainty estimate. Since the clock pulse delivery system has its own delays relative to the actual collision time and they vary from crystal to crystal, we calibrate the timing using actual relativistic particle so that their arrival time is defined to be zero. The resolution and linearity of the time measurement have been studied with test beam electrons, cosmic rays and beam splash events. Results shows that resolution is 595 ps if the pulse peak is within 10 ns range of mean measured absolute time and the linearity is verified up to 14 ns [15].

Since each photon deposit energies in a cluster of crystals, we have considered both using the timing measurement from the crystal with the highest energy deposit (seed crytal), and also a weighted average of multiple timing measurements in the cluster. Even though the latter could have a narrower rms width of the core timing distribution at zero, they are more susceptible to spurious measurements since if one measurement is "bad", the average is affected. The gain in the core resolution is negligible because significant part of the resolution is due to systematic uncertainties arising from common sources among neighbor crystals, which are not reduced by averaging. Finally, it is also easier to understand the behavior of background processes and estimates their effects on our search when we use the seed crystal timing because some of the background sources affect individual crystal differently.

Therefore, we use the timing measurements from seed crystal. However, We reject photon candidates whose timing measurements from multiple crystals are inconsistent (normalized $\chi^2 < 4$) because we are able to minimize the effect of one bad timing measurement in the seed crystal with minimum loss in the efficiency for real off-time timing measurements as the events in the left plot of (Figure 1) showing the quadratic dependence of the χ^2. They happens mostly when a particle deposit significant energy in the photo-detector itself rather than the scintillation light from the crystal which populate mostly negative times. The distribution of normalized χ^2 for time around 0 sample demonstrates that the efficiency for those photon candidates whose normalized $\chi^2 > 4$ due to timing mismeasurements of crystals is 99.2%.

There are two reasons why the photon from a neutralino arrives at ECAL later than the photons hitting ECAL directly. Many of the neutralinos are expected to be moving slower than the speed of light, so if the decay length (L1 in Figure 2) is significant, this causes delays. In addition, if the photon is emitted from the neutralino in directions much different from the neutralino direction as illustrated in Figure 2, the two paths, L1 and L2, will be much longer than the direct path, L3, from the main interaction point to the same ECAL crystal. In order to show this, we calculate Δt_1 and Δt_2 which represent delays in the photon arrival due to these two reasons and defined below.

- $\Delta t_1 = (L1/c\beta) - (L1/c)$
- $\Delta t_2 = (L1 + L2 - L3)/c$

Figure 3 shows a scatter plot of these quantities for a sample of Monte Carlo events where neutralinos are produced. The mass of neutralino is 256 GeV and the neutralino lifetime is 20
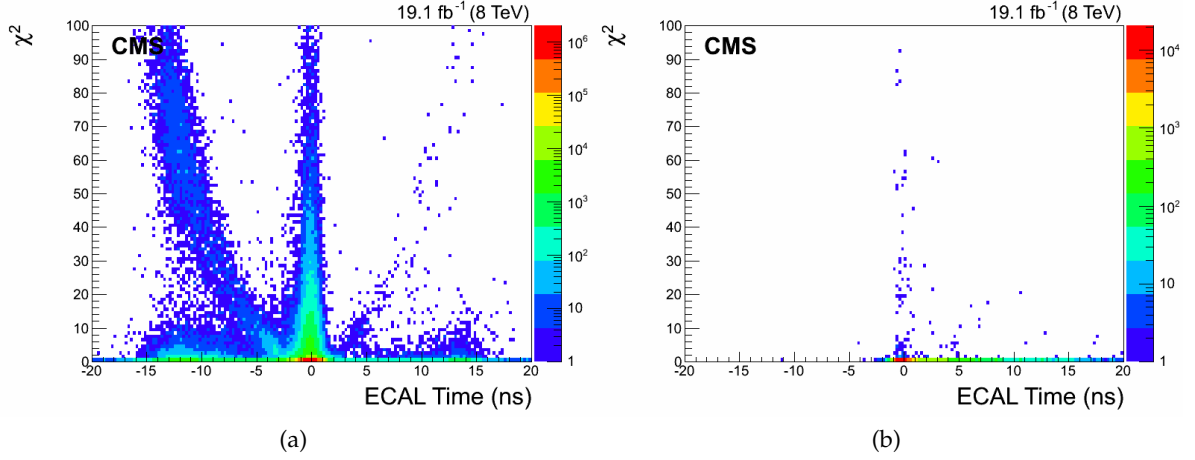
Figure 1: The correlation between ECAL time of seed crystal and χ^2 of the cluster. The quadratic-like correlation in data (left plot) indicates the inconsistence in the timing measurements from seed crystal and other cyrstals in the cluster. MC samples (right plot) do not show this correlation for out-of-time photons.
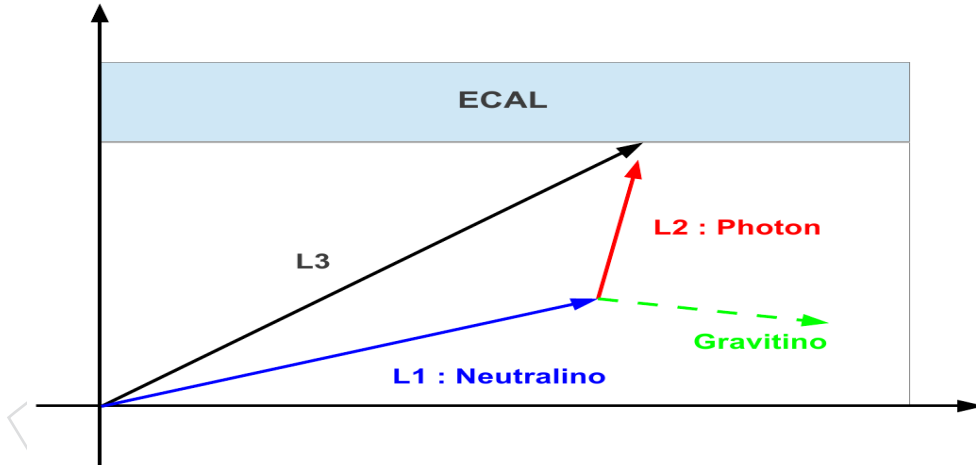

Figure 2: The schematic drawing of long-lived neutralino decay. The normal photon reconstruction uses L3 as its trajectory. L1 is the decay length of neutralino and L2 is the real photon trajectory.

ns. Since the radius of CMS ECAL is about 1.5 m which is smaller than the decay length in this scenario, those neutralino which decay inside ECAL tend to have small transverse momenta (less time dilation), and the slowness of the neutralino is the main cause of late photons as indicated by the red region along the abscissa in Figure 3.

5 Efficiencies

Because the barrel ECAL is 1.5 meters in radius, the efficiency to detect photons from neutralino decays is highly dependent on the transverse decay length (perpendicular to the proton beam direction) of the neutralino in the CMS lab frame. Figure 4a shows our estimates of efficiencies of photon reconstruction and photon selection as a function of the neutralino decay length.
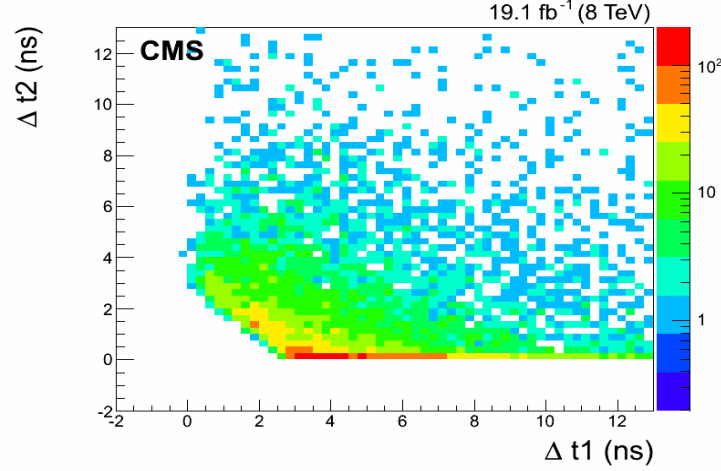
Figure 3: Δt_1 and Δt_2 distribution of GMSB sample (Λ 180 TeV and $c\tau$ 6 m) with ECAL time $>$ 3ns

The efficiency drops sharply around the decay length of 1.5 m which corresponds to where the outer surface of ECAL detector is. It shows little variation among different lifetime models at the same SUSY breaking scale.

Figure 4b shows that the efficiency decreases for the same lifetime if the SUSY breaking scale Λ decreases. This is because if the neutralino mass is heavier, the p_T of the photon and the missing energy due to the undetected gravitino are harder and more decays pass our photon p_T and E_T^{miss} requirements.
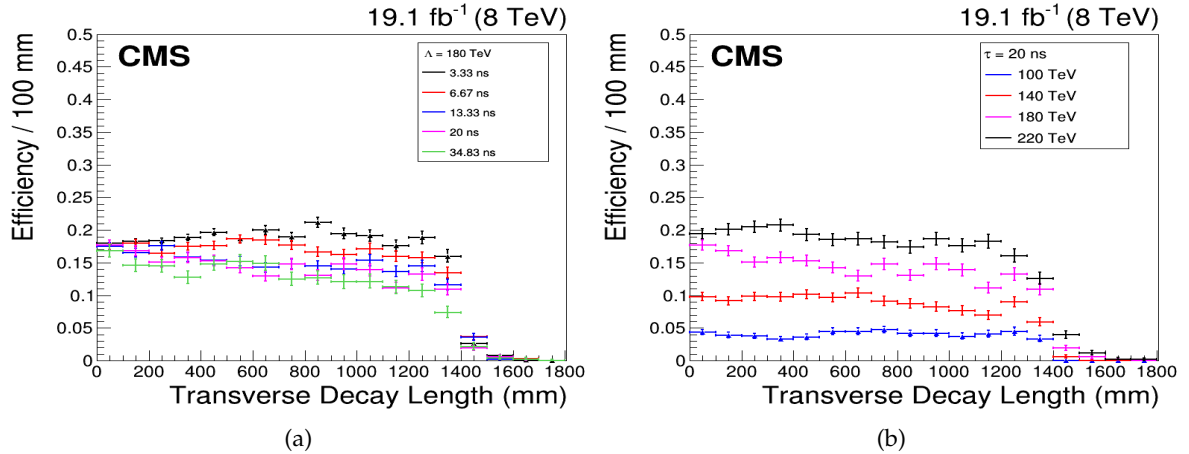

(a)

(b)

Figure 4: The efficiency of reconstruction and event selection with respect to transverse decay length for different lifetimes at Λ 180 TeV (left). Under the same lifetime scenario ($\tau = 20$ ns), the efficiency shows dependence on SUSY breaking scale (right plot).

Figure 5a shows the time acceptance of ECAL time selection for photons that they arrives later than the collision by 3 ns or more as a function of the neutralino transverse decay length. The time acceptance is higher for longer lifetime. This is because for larger lifetime scenario, we are more sensitive to lower p_T neutralinos which there are more of. The acceptance peaks around 1 m and levels off above 1.4 m or even starts increasing again. This observation can be explained using the two mechanisms for the photon from the neutralino decay to delay

as discussed in section 4. Figure 5b shows the acceptance when $\Delta t_2 < 0.5$, *i.e.* the delay is mainly due to the slowness of the neutralino, and $\Delta t_2 > 0.5$, i.e. the delay is mainly due to the long paths of the neutralino and photon. The acceptance of the former increases monotonically while the latter peaks around 0.8 m.
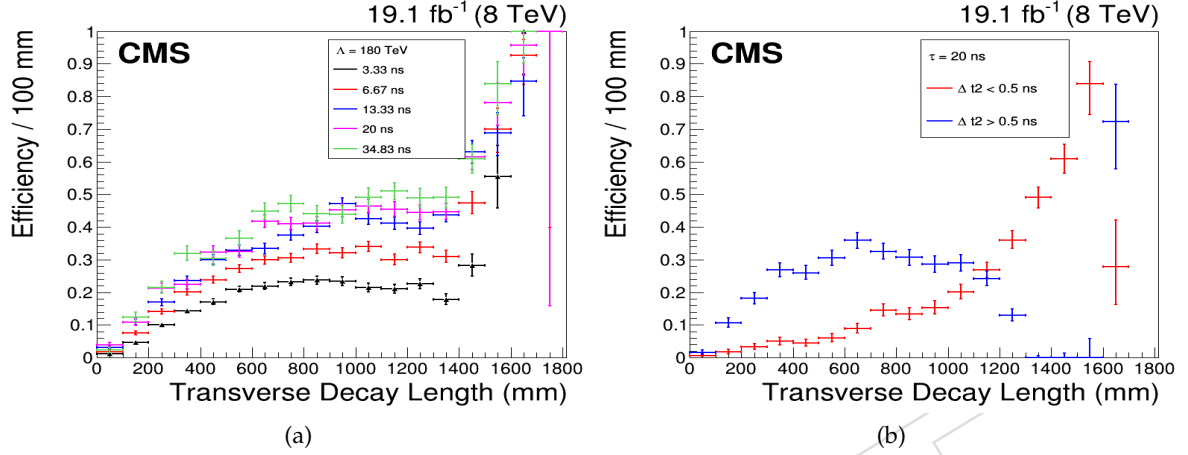

(a) (b)

Figure 5: The photon time acceptance ($t > 3$ ns) as a function of the transverse decay length in different lifetime models (left). The acceptance has two components where the main cause of the delay is the slowness of the neutralino ($\Delta t_2 < 0.5$ ns, red) and large decay angle ($\Delta t_2 > 0.5$ ns, blue)

6 Background Estimation

The main sources of delayed photons are photon candidates which are not from normal collisions. We compare an in-time photon sample ($|t| < 1$ ns) as well as an off-time photon sample ($t > 2$ ns and $t < -3$ ns) and conclude that three major background sources are beam halo, cosmic-rays and ECAL spikes. Methods to identify photons arising from them are developed using the off-time sample. The residual of non-collision background and collision backgrounds are estimated using the so-called the ABCD method. An additional estimation of collision background using Z events shows that its contribution is negligble.

6.1 Halo Photon

Beam halo muons are created when a beam proton collides with beam gas or scratches collimator upstream of CMS. They travel in the proton beam optics where because their momenta are lower than the beam protons, they get overbent by the dipole magnets and tend to be deflected in the horizontal plane once the effects for quadrupole and other magnets are taken into account. Some of these muons approach ECAL more or less in parallel to the proton beams, and radiate photons near or in ECAL. Since they are created by halo muons, a muon track segment is often found in the Cathode Strip Chambers (CSC) of the Endcap muon system which covers the same radial region as the barrel ECAL. Figure 6 shows a clear matching between a track segment found in CSC and ECAL cluster for a large fraction of the off-time events.

The timing of the arrival of these halo-induced photons show a very characteristic η dependence. A simple approximation for the arrival timing of the halo induced photon relative to photons produced in p-p interactions is given by:
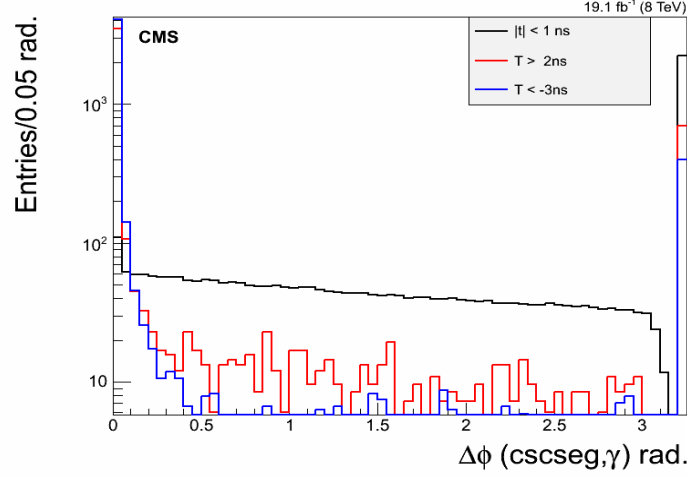
Figure 6: CSC $\Delta\phi$ distributions of in-time (black) and off-time (red and blue) samples. The events in the last bin are those without any CSC segment information available.

$$t_{ECAL} = \frac{\rho}{c}\left(\frac{1}{\tan\theta} - \frac{1}{\sin\theta}\right) \tag{3}$$

$$= -\frac{\rho}{2c}\tan(\theta/2) = -\frac{\rho}{2c}\exp^{-\eta} \tag{4}$$

where ρ is the transverse radius with respect to beam pipe, r is the distance between the main interaction point and photon cluster, z is the z position of the photon cluster, c is the speed of light, and θ is the polar angle.

The above result predicts that the ECAL arrival time of halo-induced photons is a function of η and always ealier than the time of normal photons from the associated bunch crossing. The 2D distribution of ECAL timing vs η for data in Figure 7a shows that there are a number of photon candidates which exhibit the η-ECAL timing correlation derived above and indicated by two red curves.

Due to the 400 MHz RF frequency of the LHC, it provides 9 additional LHC buckets for protons to fill beside each of the nominal LHC RF buckets. These so-called satellite bunches are thus formed when a part of proton beam is captured in one of these incorrect RF buckets at each stage of beam transfers from an earlier accelerator to the later one. The existence of satellite bunch halo can be observed from the Endcap ECAL system and identified by selecting the photon clusters each of which is matched to a CSC segment. A clear pattern of 2.5 ns structure can be seen in Figure 7b. Because CSC does not cover most of the high η region of the endcap ECAL, the efficiency for finding a CSC match for these photons is low and limited to the low η part of the endcap ECAL. This suggests that the halo from these satellite proton beams are expected to contribute photons which arrive later than the photons from the main bunch collisions.

Using the off-time control sample, we find that most halo-induced photons are associated with a CSC track segment. Therefore, a photon would be vetoed if a CSC segment with $|\eta| > 1.6$ is found within 0.05 rad of the azimuthal angle with the photon cluster. A 91% veto efficiency and 3% mis-tagging rate are found by applying this requirement.
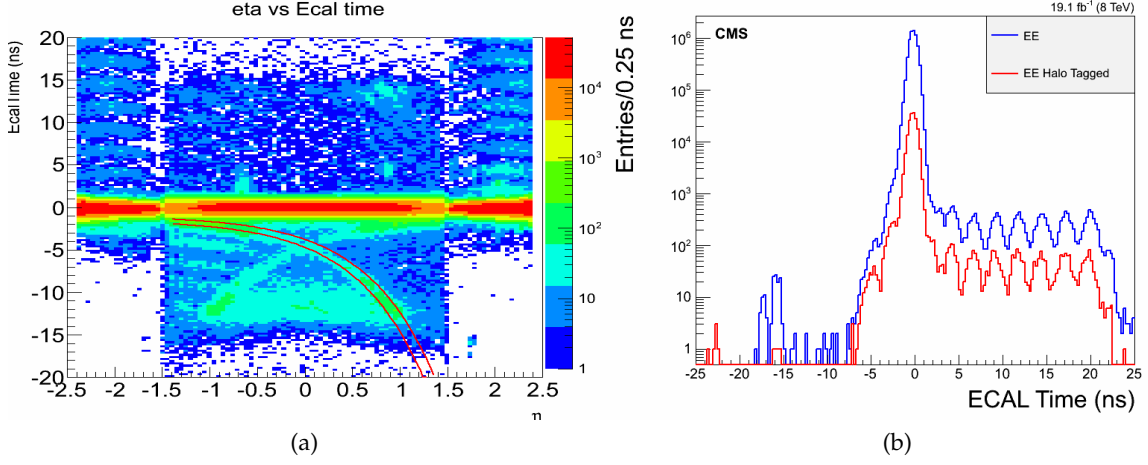
(a)

(b)

Figure 7: The η vs ECAL time for inclusive photon samples (left). The red curves show the fitting range to select halo control sample. The ECAL time of photons from ECAL Endcap (right). The periodic pattern is from the halo of satellite bunches. The red histogram is the ECAL time from photons tagged by CSC$\Delta\phi$.

6.2 Cosmic-Ray

Like halo muons, cosmic-ray muons can initiate showers in ECAL. Their existence can be found by looking at the $\Delta\phi$ and $\Delta\eta$ between a DT cosmic-ray muon segment [16] and an ECAL cluster. Due to the large space between Muon Barrel system and ECAL, the actual DT positon used in the difference calculation is a projection of the muon trajectory using the direction of the DT segment to the outer surface of ECAL. Figure 8b shows the $\Delta\phi$ and $\Delta\eta$ 2D distribution for the off-time sample where there is a clear enhancement at the small $\Delta\phi$ and $\Delta\eta$ corner of the plot while Figure 8a does not show such an enhancement for in-time sample. This demonstrates that the off-time sample contains significant fraction of cosmic muon-induced photon candidates.

(a) In-time

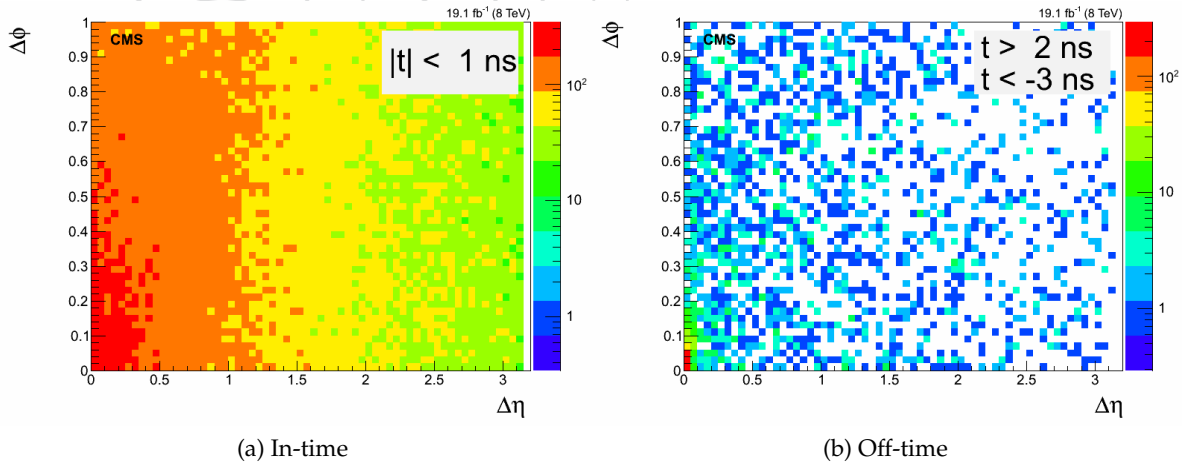(b) Off-time

Figure 8: DT $\Delta\eta - \Delta\phi$ distributions of in-time (left) and off-time (right) photon samples.

To confirm this finding, we use a cosmic dataset (no proton beams are colliding) to produce Figure 9. When there is one or more DT track segment and one ECAL supercluster in an events, we observe that 75.5% of those superclusters are associated with the projection of DT track

240 segment within the range of $|\Delta\eta| < 0.1$ and $|\Delta\phi| < 0.1$. Since these events are triggered by DT
241 hits, this tagging rate should be considered an upper limit for the efficiency. Using the normal
242 photon sample from diplaced photon dataset where the events pass the regular event selection
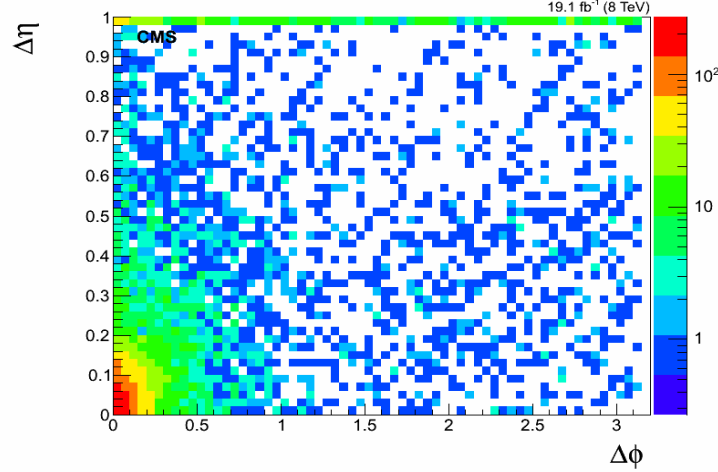243 and the ECAL time is within 1 ns window ($|t| < 1$ ns), we obtain a mis-tagging rate of 1.4%.

Figure 9: The $\Delta\eta$ and $\Delta\phi$ distribution of DT segment and ECAL supercluster for cosmic-ray data.

244 ## 6.3 Anomalous ECAL Spike

245 ECAL spikes are due to direct energy deposit by particle in the Avalanche Photo-Diode (APD)
246 [17] which is attached to $PbWO_4$ crystal to collect photons. They are often isolated apparent
247 energy deposits in one crystal, and can be rejected if the spike candidate energy (E1) and the
248 sum of its neighboring four crystals (E4) satisfies equation 5

$$1 - \frac{E4}{E1} > 1 - (0.04 \times \log E1 - 0.024) \tag{5}$$

249 while E1 greater than 4 GeV. It also will not be used to form a cluster in PF reconstruction
250 process. Occasionally, however, some of the spike hits are surrounded by some energy deposits
251 either by coincidence, or the charge particle which created the spike hit is associated with other
252 particles which deposit sufficient energies so that it is not considered a spike. This component
253 can be identified in the negative timing sample where we don't find any correlation with muon
254 system segments for either halo-induced photons or cosmic muon-induced photons.

255 Due to its production mechanism, when a non-isolated spike hit forms an ECAL cluster, its size
256 is expected to be smaller than the size of regular photons. Figure 10 shows the distribution of
257 S_{Major} vs S_{Minor} for the above spike-enhanced sample. The dense area at small S_{Major} as well as
258 S_{Minor} is due to spikes since they are not accompanied by energetic hits very often. The "swiss-
259 cross" values for the spike-enhanced sample is also compared with the values from nominal
260 photon sample. It also indicates higher swiss-cross values for spike-enhance sample. Based
261 on these observations, we use a tigher swiss-cross cut ($1-\frac{E4}{E1} > 0.9$). In addition, we also veto
262 photons with $S_{Major} < 0.6$ and $S_{Minor} < 0.17$.
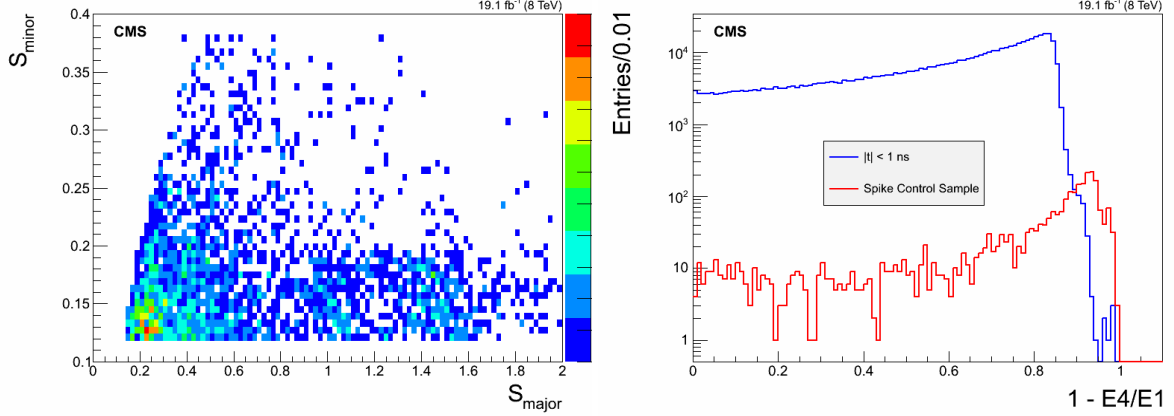
Figure 10: S_{Major} and S_{Minor} distribution of spike control sample.

6.4 ABCD Method for Non-Collision Background

By applying the methods to veto background events from three sources, we can reduce the background contributions significantly. Figure 11 shows the ECAL timing distribution of the 0 and 1-jet data sample. The plot shows three major background components which are tagged by our tagging methods. Halo contributes the most in the off-time area. Cosmic-rays and ECAL spike background also have expected shape from the tagged components. However, the remaining photons after removing all the tagged backgrounds still have significant number of photons with $|t| > 3$ ns since the tagging efficiencies are not 100%. We use the so-called ABCD method to estimate how many of these photons are due to untagged background contributions.
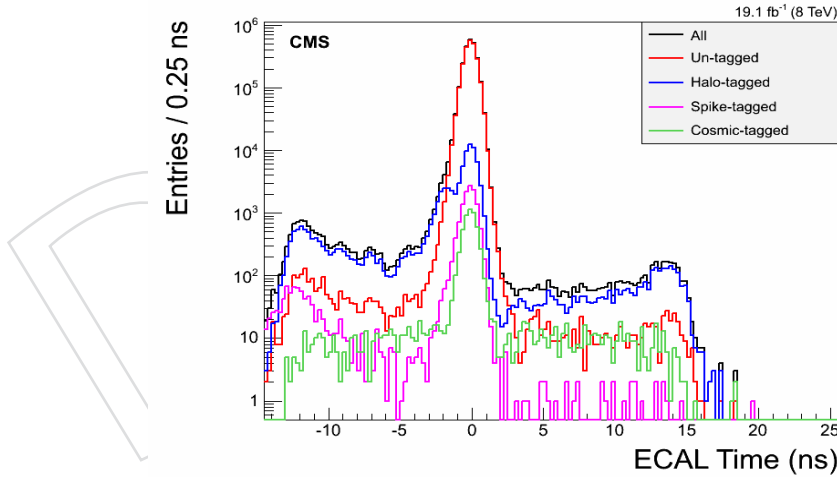

Figure 11: ECAL time distribution from 0 and 1-jet events. Three tagged background sources and the remaining are shown in different color.

We seek signal in the ECAL timing window between 3 and 13 ns and $E_T^{miss} > 60$ GeV, which suppress normal photons arising from proton collisions in the regular RF buckets. Our signal events have a large E_T^{miss} since a gravitino cannot be detected. However, background photons from the three sources we have discussed in section 3 will have large E_T^{miss} since the photon does not arise from a regular collision and they will have small $E_{T\,no\gamma}^{miss}$ if taking photon out of E_T^{miss} calculation.

The ABCD regions are defined from ECAL time and $E_{T\,no\gamma}^{miss}$ which is shown in Table 3 where

279 E_T^miss is required to be greater than 60 GeV which suppresses photons from the collision-type
280 events. A and B regions are signal free region since there are no signal in $t < -3$ ns. Region C
281 ($E_\text{T no$\gamma$}^\text{miss} < 60$ GeV) is also signal free, and photons from collision should be suppressed because
282 most of them should have large $E_\text{T no$\gamma$}^\text{miss}$. Thus, the non-collision background in signal region D
283 can be estimated from

$$\text{Non-collision background in D} = \frac{B}{A} \times C \tag{6}$$

	$E_\text{T no$\gamma$}^\text{miss} < 60$ GeV	$E_\text{T no$\gamma$}^\text{miss} > 60$ GeV
$t > 3$ ns	C	D
$t < $-3 ns	A	B

Table 3: ABCD definition for non-collision background estimation. All events pass $E_\text{T}^\text{miss} > 60$ GeV requirement.

6.5   ABCD Method for Collision Background

285 As for possible contamination from collision events, another ABCD method using ECAL time
286 and E_T^miss is developed. This method is aimed as estimating the collision events in each of
287 ABCD regions defined in previous section. As collision events are suppressed in A and C region
288 and non-collision backgrounds dominate in these two regions ($E_\text{T}^\text{miss} > 60$ GeV and $E_\text{T no$\gamma$}^\text{miss} <$
289 60 GeV), this estimation is only necessary for B and D regions. We use events with $E_\text{T no$\gamma$}^\text{miss} >$
290 60 GeV to estimate collision background in these two regions to minimize non-collision back-
291 ground. Since ECAL time from collision type events should be around zero, the $|t| < 2$ns region
292 can be used as the control region to extract ratio for collision events with large and small E_T^miss
293 values. The ABCD regions are defined in Table 4. The collision background in D region is
294 estimated by

$$Q_d(\text{Collision background in D}) = \frac{F}{F'} \times D' \tag{7}$$

295 Similar to the collision background in D, the same formula is also applicable to B region.

$$Q_b(\text{Collision background in B}) = \frac{F}{F'} \times B' \tag{8}$$

	$E_\text{T}^\text{miss} < 60$ GeV	$E_\text{T}^\text{miss} > 60$ GeV
$t > 3$ ns	D'	D
$|t| < 2$ ns	F'	F
$t < $-3 ns	B'	B

Table 4: ABCD Region definition for collision background estimation. All events pass $E_\text{T no$\gamma$}^\text{miss} > 60$ GeV requirement.

6.6   Collision Background From Z Events

297 Another approach using $Z \to e^+e^-$ events to estimate the background contribution from colli-
298 sion event is studied. We use events with at least two electrons with p_T greater than 30 GeV.
299 The electron isolation is not applied because the algorithm handles off-time ECAL crystals in-
300 appropriately for our purpose in isolation energy calculation. We use the distinct Z mass peak

in the invariant mass distribution of two electrons and count the excess number of di-electron pairs in the range between 76 GeV and 104 GeV to estimate in-time and late electrons.

The goal is to estimate the probability that the timing measurement of an electron from the Z sample is out-of-time ($t > 3$ ns or $t < 3$ ns). It represents the probability to mis-measure an object from in-time collision. Therefore, we define three samples based on the timing of the electrons from the Z sample.

- In-time events. Both electrons are within $|t| < 2$ ns region (Figure 12).
- Late timing events. The arrival time of at least one of the electron is $t > 3$ ns (Figure 13a).
- Early timing events. The arrival time of at least one of the electron is $t < $ -3 ns. If one electron is early and the other is late, the event is classified as late timing (Figure 13b).

In order to estimate the number of Zs in each of the above sample, we first fit the sideband (50 to 76 GeV and 104 to 130 GeV) with a forth order polynomial function to estimate the background under the Z peak. By subtracting the background represented by the integral of the background function in the peak region, we can estimate the number of pure Z events in these samples.

The resulting number of Z events in the three time intervals are listed in Table 5. Of those 32.4 Z candidates with at least one of the electrons are measured to be late, three of them have both electrons late, presumably because these Zs are produced in satellite bunch collisions. Since satellite bunch intensity is roughly 10^{-3} times the main bunch intensity, their collision luminosity is expected to be 10^{-6} [18]. This is consistent with the observed three Z candidiates with late electron daughters out of 1.35 million in-time Zs. Therefore, we separate these three events and calculate the probability of a late timing measurement ($29.4/1352383.4 = (1.09 \,^{+0.28}_{-0.23}) \times 10^{-5}$, denoted as p_1 in equation 9) as well as the probability of a late collision events ($3/1352383.4 = (2.22 \,^{+1.7}_{-0.96}) \times 10^{-6}$, denoted as p_2 in equation 9).

Using these probabilities, we can predict number of collision background in $t > 3$ ns by

$$N = n_1 \times p_1 + n_2 \times (2p_1(1 - p_1) + p_1^2) + n_1 \times p_2 + n_2 \times p_2 \tag{9}$$

where n_1 is the number of in-time one photon event (28208) and n_2 is the number of in-time two photon event (38) from the F region, defined in the result section. The estimated background is $0.370 \,^{+0.092}_{-0.070}$. This is larger than the result ($0.093 \,^{+0.093}_{-0.047}$) from the collision ABCD method, but both methods suggest negligible contribution (less than 1 event predicted) from collision events to off-timing region. Since this method can tell us the composition of the particle with late time measurements, we choose this as the default estimate of the background arising from collision events.

	$t < $ -3 ns	$|t| < 2$ ns	$t > 3$ ns
Total	378	2349187.0	41.0
Estimated Background	329	996803.6	8.6
Estimated Z	49	1352383.4	32.4

Table 5: The numbers of event in different time regions of Z sample (76 GeV < Mass < 104 GeV).
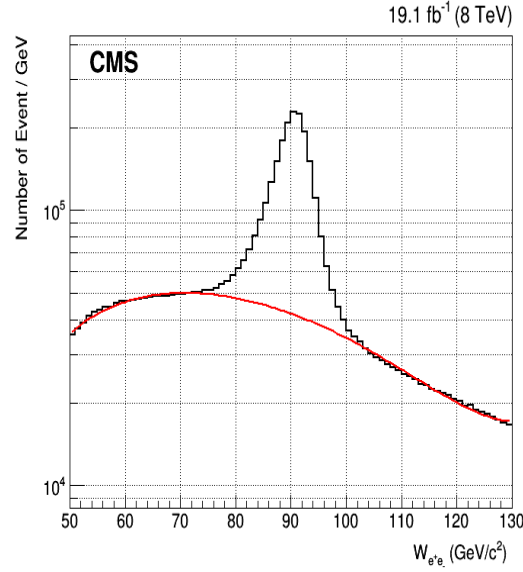
Figure 12: The invariant mass of two in-time ($|t| < 2$ ns) electrons. The red curve is the background estimation by fitting the sideband.
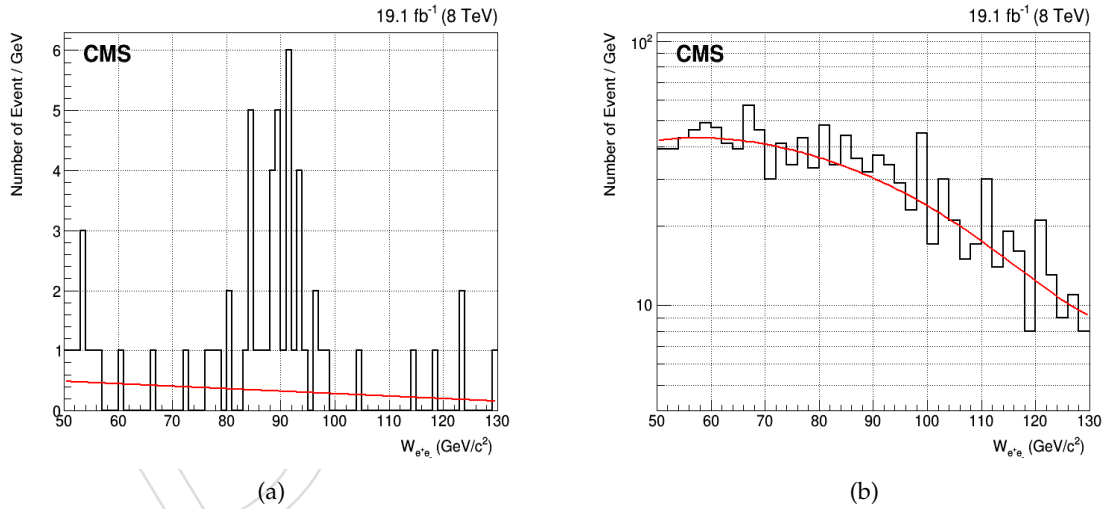

Figure 13: The Z mass distribution from late timing (left) and early timing (right) events. The red curves are the background estimation by fitting the sideband.

6.7 Combined ABCD Method and Closure Test

Based on the results of two estimations for collision background, we choose the value from $Z \to e^+e^-$ events since it suggests a larger value for collision background. Combining the non-collision and collision backgrounds, the final background in the signal region is estimated by

$$\text{Total background in D} = (\frac{B - Q_b}{A} \times C) + Q_d \tag{10}$$

$$\tag{11}$$

340 where Q_b and Q_d are the collision components in the B and D regions.

341 A closure test is done by using 0 and 1-jet events, where we don't expect any signal events, so
342 the background estimates for the D region should agree with the actual number of events in
343 the D region. The yields in each region and the number of vetoed backgrounds can be found
344 in Tables 6 and 7. The uncertainty is calculated based on the statistic nature of each region
345 and the method of Pearson's χ^2 interval [19]. The estimated background in the D region for 0
346 and 1-jet events events is 16.41 ($^{+3.00}_{-2.59}$) which is compatible with the observed value of 10. The
347 uncertainty from collision background has negligible effect because the ratio of out-of-time and
348 in-time photon is small.

$$\mathrm{D} = (\frac{38 - 0.64}{851} \times 359) + 0.46 = 16.41^{+3.00}_{-2.59} \tag{12}$$

$$Q_d = 0.46^{+0.11}_{-0.09} \tag{13}$$

$$Q_b = 0.64^{+0.35}_{-0.34} \tag{14}$$

	Spikes	Halo	Cosmic	Yield
D	0	22	27	10
C	9	1506	368	359
B	1	293	17	38
A	65	5062	235	851
F	-	-	-	35271

Table 6: Numbers used in closure test of the 0 and 1-jet events. Numbers in Spikes/Halo/Cosmic columns are the counts vetoed by corresponding background tagging in each defined region. F region is dominated by collision backgrounds. Therefore only the yield is shown.

	Spikes	Halo	Cosmic	Yield
B'	0	1	1	8
D'	0	0	0	2
F'	-	-	-	1445254

Table 7: Closure test from 0 and 1-jet events for collision background estimation. The first three columns are the vetoed backgrounds.

7   Systematic Uncertainties

350 This analysis relies on photons above 80 GeV in p_T, jet above 35 GeV in E_T and E_T^{miss} larger
351 than 60 GeV. So the efficiency estimated using MC sample must simulate these quantities well,
352 and any uncertainties on how these quantities match between data and Monte Carlo will lead
353 to systematic uncertainties in the efficiency.

354 We compare data and $\gamma+$ jets samples to study the timing simulation for photon. Both samples
355 are requiring one isolated photon, one or two jets and E_T^{miss} less than 30 GeV in events which
356 is statistically independent of the data we look for delayed photons. The difference of mean
357 value and resolution from the fit of ECAL timing distribution are applied to correct the GMSB
358 samples and considered as systmetics. In addition to ECAL timing, we also estimate the uncer-
359 tainties due to the uncertainties in the jet energy scale, jet energy resolution, electron-gamma
360 and energy scale, unclustered energy for E_T^{miss}.

We vary their 1-σ deviation with respect to the nominal values. The results are summarized in Table 8. The timing bias has most significant impact to the result since our method is a pure counting method on ECAL time. The second largest source of uncertainty comes from unclustered energy uncertainty of E_T^{miss}. It has biggest effect on the E_T^{miss} scale.

Given the same τ, the systematic uncertainties usually have higher impact to lower SUSY breaking scale cases. This is due to the fact that there are fewer events detected for lighter neutralino (i.e. smaller Λ) and the statistical uncertainties of the systematic effects are large. Photon decay from lighter neutralino has softer p_T spectrum and causes lower efficiency for passing the photon p_T requirement. In addition, ligher neutralino is more boosted than heavier neutralino, which also results in lower efficiency since there are fewer slow motion neutralinos on which our analysis relies.

Other general factors such as luminosity [20] and parton distribution function [21] are adopted from the official CMS study. These factors are all then applied in the statistic analysis as nuisance parameters.

Because the background estimation uses a pure data-driven method, most effects from these systematic uncertainties are canceled out ($< 1\%$ impact). The systematic uncertainty on background estimation is quoted as upward 105% and 19% downward by using the statistic uncertainty of the $Z \rightarrow e^+e^-$ method. Due to low statistic counts, the background uncertainty is large. However, it does not impact the final result as significantly as the uncertainties of signal efficiency.

Source	Uncertainty(%)
Time zero	$6 \sim 10$
Unclustered Energy	$4 \sim 10$
ECAL time resolution	$2 \sim 5$
Jet energy scale	$3 \sim 9$
Jet energy resolution	$2 \sim 9$
Photon energy scale	$2 \sim 4$
Luminosity	2.6
PDF	< 1

Table 8: Systematic uncertainties for signal efficiency

8   Result

Only one event is observed in the signal region. The event contains one photon and two jets. The photon in the event has transverse momentum 224 GeV and ECAL time 12.17 ns. Its S_{major} and S_{minor} are 2.82 and 0.16. The final background estimation is 0.37 ($^{+0.39}_{-0.07}$). The vetoed backgrounds and the numbers used in background estimation are presented in Table 9 and Table 10.

$$D = (\frac{1 - 0.51}{3} \times 0) + 0.37 = 0.37^{+0.39}_{-0.07} \tag{15}$$

$$Q_d = 0.37^{+0.09}_{-0.07} \tag{16}$$

$$Q_b = 0.51^{+0.28}_{-0.27} \tag{17}$$

With no significant excess events over estimated background, we find an upper limit of 4.07 photon counts at 95% C.L. using CLs method [22]. Assuming the GMSB model and the SUSY

breaking scale is 180 TeV, this corresponds to a cross section of 12.05 fb for the neutralino production of photon plus gravitino channels and the lifetime of the neutralino (τ) is either less than 3.2 ns or larger than 19.87 ns (Figure 14).

Taking GMSB as a benchmark model, the exclusion region at 95% C.L. in neutralino mass is up to 300 GeV. The excluded lifetime range is about 2 ns to 40 ns for low mass neutralino and the excluded interval shrinks when the mass increases (Figure 15). This is mainly due to smaller expected cross-section of neutralino production at higher Λ (or neutralino mass) values.

	Spikes	Halo	Cosmic	Yield
D	0	0	0	1
C	0	2	1	0
B	1	1	1	1
A	0	6	0	3
F	-	-	-	28246

Table 9: Final background estimation for signal candidates. All events pass $E_T^{miss} > 60$ GeV cut.

	Spikes	Halo	Cosmic	Yield
B′	0	0	0	3
D′	0	0	0	1
F′	-	-	-	604958

Table 10: Final background estimation for at least one photon and two jets events. All events pass $E_T^{miss} > 60$ GeV cut.
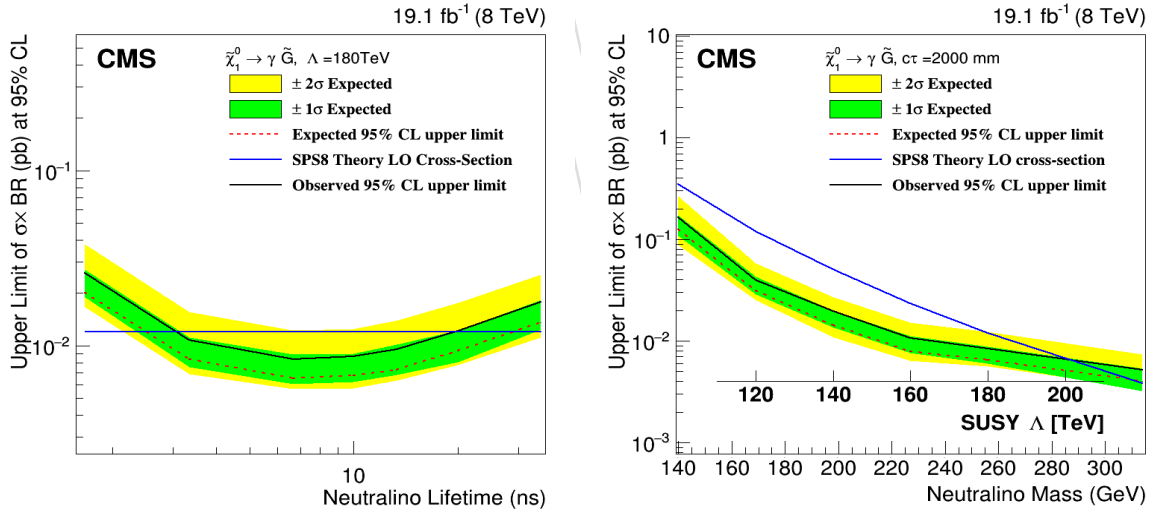

Figure 14: Upper limit at 95 % C.L. for Λ 180 TeV in different lifetime and τ 67 ns in different Λ values using CL_s method

9 Conclusion

We develop an effective method using ECAL timing to search for delayed photon signal in the CMS experiment. We apply it to long-lived neutral particle decaying to a photon and gravitino using the data with an integrated luminosity 19.1 fb^{-1} from the LHC proton-proton collision
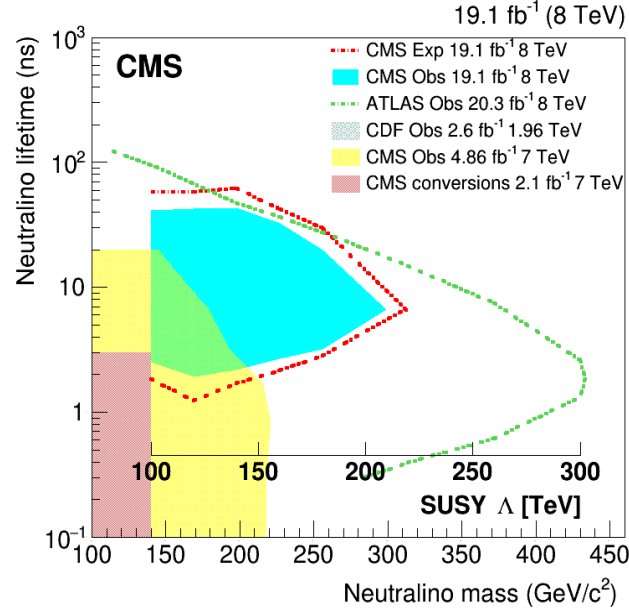
Figure 15: Exclusion region for the mass and lifetime of neutralino in the SPS8 model

at 8 TeV center-of-mass energy in 2012. The upper limit of cross-section times branching ratio is obtained with respect to different lifetime and mass of the neutral particle (Figure 16). Comparing with the previous searches [7, 8] in CMS experiment, the CMS ECAL timing method provides broader search spectrum for long-lived neutralinos.
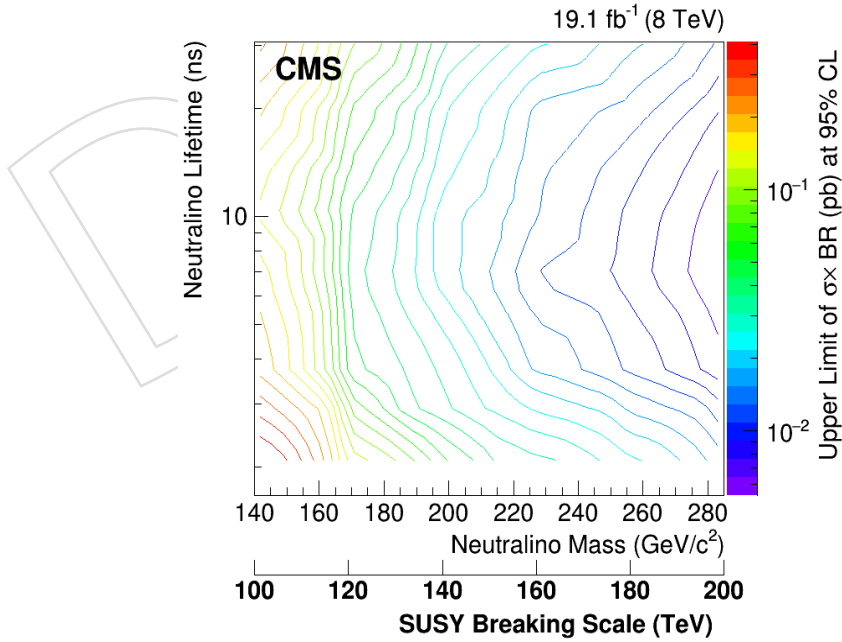

Figure 16: Cross-section limit for the mass and lifetime of neutralino using 8 TeV data with integrated luminosity $19.1\,\text{fb}^{-1}$ from the CMS experiment

References

[1] N. Seiberg, "Naturalness versus supersymmetric non-renormalization theorems", *Phys. Lett. B* **318** (Oct, 1993) 469–475. 14 p.

[2] G. F. Giudice and R. Rattazzi, "Theories with Gauge-Mediated Supersymmetry Breaking", *Phys. Rep.* **322** (Jan, 1998) 419–499. 103 p.

[3] S. P. Martin, "A Supersymmetry Primer",.

[4] B. C. Allanach et al., "The Snowmass Points and Slopes: Benchmarks for SUSY Searches", *Eur. Phys. J. C* **25** (Feb, 2002) 113–123. 12 p.

[5] L. Covi, J. Hasenkamp, S. Pokorski, and J. Roberts, "Gravitino Dark Matter and general neutralino NLSP", *J. High Energy Phys.* **11** (Aug, 2009) 003. Comments: 30 pages, 15 figures, pdflatex.

[6] CDF Collaboration Collaboration, "Search for Supersymmetry with Gauge-Mediated Breaking in Diphoton Events with Missing Transverse Energy at CDF II", *Phys.Rev.Lett.* **104** (2010) 011801, `doi:10.1103/PhysRevLett.104.011801`, `arXiv:0910.3606`.

[7] CMS Collaboration Collaboration, "Search for long-lived particles decaying to photons and missing energy in proton-proton collisions at $\sqrt{s} = 7$ TeV", *Phys.Lett.* **B722** (2013) 273–294, `doi:10.1016/j.physletb.2013.04.027`, `arXiv:1212.1838`.

[8] CMS Collaboration Collaboration, "Search for new physics with long-lived particles decaying to photons and missing energy in pp collisions at $\sqrt{s} = 7$ TeV", *J. High Energy Phys.* **11** (Jul, 2012) 172. 29 p.

[9] ATLAS Collaboration Collaboration, "Search for non-pointing and delayed photons in the diphoton and missing transverse momentum final state in 8 TeV *pp* collisions at the LHC using the ATLAS detector", *Phys. Rev. D* **88** (Apr, 2013) 012001. 26 p.

[10] T. Sjöstrand, S. Mrenna, and P. Skands, "PYTHIA 6.4 physics and manual", *JHEP* **05** (2006) 026, `doi:10.1088/1126-6708/2006/05/026`, `arXiv:hep-ph/0603175`.

[11] P. Z. Skands et al., "SUSY Les Houches Accord: Interfacing SUSY Spectrum Calculators, Decay Packages, and Event Generators", *J. High Energy Phys.* **07** (Nov, 2003) 036. 29 p.

[12] CMS Collaboration Collaboration, "Photon reconstruction and identification at sqrt(s) = 7 TeV", Technical Report CMS-PAS-EGM-10-005, CERN, 2010. Geneva, 2010.

[13] for the CMS Collaboration Collaboration, "The CMS Particle Flow Algorithm",. Comments: 10 pages, 12 figures, proceedings for CHEF2013, Paris, France, April 2013.

[14] CMS Collaboration Collaboration, "Jet Performance in pp Collisions at 7 TeV", Technical Report CMS-PAS-JME-10-003, CERN, Geneva, 2010.

[15] CMS Collaboration Collaboration, "Time Reconstruction and Performance of the CMS Electromagnetic Calorimeter", *J. Instrum.* **5** (Nov, 2009) T03011. 27 p.

[16] N. Amapane et al., "Local Muon Reconstruction in the Drift Tube Detectors",.

[17] CMS Collaboration, "Characterization and treatment of anomalous signals in the CMS Electromagnetic Calorimeter", *AN-10-357* (2011).

442 [18] A. Jeff et al., "Measurement of Satellite Bunches at the LHC", *Conf. Proc.* **C1205201** (May, 443 2012) MOEPPB010. 3 p.

444 [19] J. G. Heinrich, "Coverage of Error Bars for Poisson Data",.

445 [20] CMS Collaboration Collaboration, "CMS Luminosity Based on Pixel Cluster Counting - 446 Summer 2013 Update", Technical Report CMS-PAS-LUM-13-001, CERN, Geneva, 2013.

447 [21] S. Alekhin et al., "The PDF4LHC Working Group Interim Report", Technical Report 448 arXiv:1101.0536, Jan, 2011. Comments: 35 pages.

449 [22] A. L. Read, "Modified frequentist analysis of search results (the CL_s method)",.